Research article

Enzyme-loaded manganese−porphyrin metal−organic nanoframeworks for oxygen-evolving photodynamic therapy of hypoxic cells

Yang Qiao [a], Xiaowan Tang [a], Xu Qiuju [b], Guangwen Zhang [a,*]

[a] *Department of Hematology and Oncology, Wenzhou Medical University affiliated Huangyan Hospital, The First People's Hospital of Taizhou, People's Republic of China*
[b] *The Third Affiliated Hospital of Harbin Medical University, 150 Haping Rd, Harbin, Heilongjiang Province, People's Republic of China*

ARTICLE INFO

ABSTRACT

Photodynamic therapy (PDT) is attracting great attention for cancer treatments, while its therapeutic efficacy is limited by unsatisfactory photosensitizers and hypoxic tumor microenvironment (TME). To address these problems, we have developed catalase-loaded manganese-porphyrin frameworks (CAT@MnPFs) for catalytically-assisted PDT of cancer cells. CAT@MnPFs were constructed by the assembly of Mn^{2+} ions and PpIX into MnPFs and the subsequent loading of catalase. Under 650 nm light irradiation, the porphyrin (Protoporphyrin IX) within the structure of CAT@MnPFs can convert oxygen (O_2) into singlet oxygen ($^1O_2$), showing the photodynamic effect. Importantly, the loaded catalase can decompose hydrogen peroxide (H_2O_2) into O_2 with a huge elevation of O_2 level (13.22 mg L^{-1}) in 600 s, thus promoting $^1O_2$ generation via PDT. As a result, CAT@MnPFs combined with 650 nm light can effectively ablate cancer cells due to the catalase-assisted oxygen-evolving PDT, showing a high therapeutic efficacy. Meanwhile, after the incubation with CAT@MnPFs, unobvious damage can be found in normal and red blood cells. Thus, the obtained CAT@MnPFs integrate the advantage of photosensitizers and catalase for oxygen-evolving PDT, which can provide some insight for treating hypoxic cells.

1. Introduction

Photodynamic therapy (PDT) is a new method that uses photosensitizers and light activation to treat tumors. In the presence of O_2, photosensitizers combined with light can generate cytotoxic reactive oxygen, such as singlet oxygen ($^1O_2$), leading to cell oxidative death [1]. The prerequisite for PDT is photosensitizers that mainly include inorganic photosensitizers (e.g., Au–TiO_2 [2], $MnWO_X$ [3], etc.), organic photosensitizers (porphyrin derivatives [4], artemether [5], etc.), and metal-organic frameworks (MOF) photosensitizers (e.g. ZIF-8 [6], Mn-IR825 [7], MFe_2O_4 (M = Mn, Co, or Zn) [8,9], Ti-TCPP [10], Cu-HMME [11], Zr-thiazolothiazol [12], etc.). Inorganic photosensitizers usually suffer from complex synthesis and difficult degradation, leading to long-term safety concerns. Some organic photosensitizers are always used as pharmaceutical formulations due to their low solubility, which has to be loaded on nanocarriers, resulting in low loading efficiency and easy leaking in physical conditions. Unlike simple packaging, photosensitizers of MOF incorporate organic photosensitizers and metal ions as their construction units [13,14], isolating photosensitizers to reduce their

---

self-quenching. Meanwhile, MOFs-based photosensitizers can also facilitate the diffusion of O_2 and the freshly generated $^1O_2$ [13]. However, tumor microenvironment (TME) is characterized by hypoxia due to the uncontrolled proliferation of cancer cells, and the PDT-mediated continuous consumption of O_2 will exacerbate the hypoxic level. Additionally, the therapeutic effect of PDT firmly depends on the surrounding oxygen environment, and severe hypoxia is highly detrimental to the therapeutic effect of O_2-dependent PDT. Therefore, it is necessary to develop photosensitizers that can overcome hypoxia and efficiently produce $^1O_2$ to kill cancer cells.

To address hypoxia, there are serval strategies including carrying oxygen directly and *in situ* O_2 generation inside tumors [14]. To deliver O_2, transporters into tumors have been reported such as hemoglobin, red blood cell-derived vesicles, and perfluorocarbon microbubbles [15]. For the *in situ* generation of O_2, intracellular hydrogen peroxide (H_2O_2) is overexpressed in the TME, which provides an opportunity for catalysts or enzymes that can catalyze the decomposition of H_2O_2 into O_2 [16–18]. For example, manganese dioxide (MnO_2) has been recognized as a mimic enzyme that can convert H_2O_2 into water and O_2 with high O_2 generation efficiency [19]. The mimic enzymes (MnO_2, platinum, and palladium) can sustainably relieve hypoxic TME, and they also suffer from limitations such as difficult degradation, bad biocompatibility, size-dependence, and complicated synthesis procedures, raising some metabolic problems [20]. Notably, catalase derived from bovine serum is self-reactivity to H_2O_2, showing high catalytic efficiency, strong substrate affinity, and good biocompatibility [21]. Then catalase can ameliorate the hypoxic TME and improve O_2-dependent PDT efficacy. However, natural catalase can be easily destroyed by physiological proteases during blood circulation [22], leading to poor *in vivo* half-life [23], which needs suitable nanocarriers to deliver and protect it. Thus, it is desired to design novel therapeutic agents that integrate photosensitizers and catalase for better PDT outcomes.

Porphyrin-based MOFs with high porosity and biodegradability have been designed as efficient photosensitizers for PDT and as carriers to load a variety of therapeutic agents (e.g., chemotherapeutics, siRNA, enzymes) [24]. Encouraged by these, it can be proposed that catalase can be encapsulated into porphyrin-based MOF for catalase-assisted PDT. Herrin, we prepared Mn-PpIX (Protoporphyrin IX, a traditional photosensitizer) frameworks (MnPFs, ~100 nm) that not only serve as photosensitizers to generate $^1O_2$ for PDT but also act as the carrier to load catalase (CAT) for alleviation of hypoxia, boosting PDT process (Scheme 1). Under the 650 nm light irradiation, CAT@MnPFs can trigger $^1O_2$ generation and induce degradation of 19.1 % 1.3-diphenyl isobenzofuran (DPBF) within 30 s. Additionally, in the presence of H_2O_2, CAT within CAT@MnPFs greatly increases the O_2 concentration with a huge elevation (13.22 mg L^{-1}) in 600 ms, thereby facilitating the production of $^1O_2$ that is nearly three times as much as in the group without H_2O_2. After the incubation with CAT@MnPFs, the hypoxia of 4T1 cells was alleviated and the cell oxidative death was triggered under light irradiation, achieving catalytically-assisted PDT. In addition, after the incubation with CAT@MnPFs, unobvious damage can be found in normal and red blood cells.

2. Experimental methods

2.1. Materials

Protoporphyrin IX (PpIX), $MnCl_2 \cdot 4H_2O$, methanol, trimethylamine, N, N-dimethylformamide (DMF), 1.3-diphenyl isobenzofuran (DPBF) were received from Sinopharm Chemical Reagent Co., Ltd. Calcein-AM, propidium iodide (PI), 20,70-Dichlorofluorescin diacetate (DCFH-DA), 4′,6-diamidino-2-phenylindole (DAPI), cell counting kit-8 (CCK-8) assay, phosphate buffer saline (PBS) were obtained from Beyotime Biotechnology.

2.2. Synthesis of CAT@MnPFs

CAT@MnPFs were prepared through two steps. Firstly, methanol/trimethylamine solution (20 mL, 50/1 vol%) containing 5 mg PpIX was mixed with the methanol/DMF solution (10 mL, 85/15 vol%) which includes 10 mg $MnCl_2 \cdot 4H_2O$, with stirring for 2 h at 25 °C. The mixture was placed in an ultrasonic cleaning instrument (40 KHz) for 4 h and centrifuged at 12,000 rpm for 20 min to obtain MnPFs. Then, catalase (0.2 mL, ≥30,000 units per mL) was added into the MnPFs solution (5 mL, 1 mg mL^{-1}) with stirring

Scheme 1. Schematic of CAT@MnPFs for boosting PDT process.

overnight. The excess CAT was removed after centrifugation (12,000 rpm, 20 min), thus obtaining CAT@MnPFs.

2.3. Catalytic activity

The MnPFs (10 mL, 50 µg mL^{-1}) and CAT@MnPFs (10 mL, 50 µg mL^{-1}) were placed in a 37 °C water bath with continuous stirring. Catalase catalytic activity is reflected in the decomposition of H_2O_2 into O_2, which induces the change in dissolved oxygen concentration. H_2O_2 (1 mM) was introduced into the above solutions with stirring. The dissolved oxygen concentration was monitored in real time by a portable dissolved oxygen meter.

2.4. $^1O_2$ detection

The DPBF was selected as a probe to detect the generation of $^1O_2$ by the CAT@MnPFs [25]. Briefly, a DMF solution containing DPBF (10 µL, 2 mg mL^{-1}) was added into CAT@MnPFs solution (2 mL, 20 µg mL^{-1}). Then the mixture was exposed to 650 nm light (100 mW cm^{-2}) for 30 s and the UV–vis photoabsorption was recorded at 0, 5, 10, 15, 20, and 30 s. To measure the effect of H_2O_2 on $^1O_2$ generation, H_2O_2 (1 mM) was added into the 2 mL solution which contained DPBF (20 µg mL^{-1}) and the CAT@MnPFs (40 µg mL^{-1}). After irradiation by light, the photoabsorption of the mixture was also monitored by a UV–vis spectrometer for 30 s duration.

2.5. Cytotoxicity and uptake in vitro

Murine breast cancer 4T1 cells (4T1) were cultured with the RPMI-1640 medium containing 10 % FBS and 1 % penicillin–streptomycin. For cytotoxicity assay, 4T1 cells (1×10^4 cells in each well) were seeded into the 96-well plates and cultured for 24 h in the dark. Then the culture medium was added with CAT@MnPFs solutions at a series of concentrations (0, 50, 100, 150, 200, and 300 µg mL^{-1}) and the cells were cultured for another 24 h. After incubation, cell viability was determined by a standard CCK-8 assay. For uptake assay, the medium containing CAT@MnPFs (200 µg mL^{-1}) was used to culture 4T1 cells for 0.5, 2, 4, 8 h, respectively. After washing by PBS, the 4T1 cells were stained with 4′, 6-diaminidine −2 phenylindole (DAPI) for 20 min, followed by imaging under a fluorescence microscope. All experiments were independently performed four times.

2.6. Intracellular O_2 and ROS detection

The O_2 level in 4T1 cells was detected by an optical probe, $[Ru(dpp)_3]Cl_2$ whose red luminescence could be quenched by O_2. 4T1 cells were cultured at 37 °C under a hypoxia condition (1 % O_2). After 24 h, $[Ru(dpp)_3]Cl_2$ (0.1 µM) was added into the medium and incubated for another 6 h. Then the treated cells were incubated with CAT@MnPFs (200 µg mL^{-1}) and H_2O_2 (100 µM) for 4 h. Intracellular O_2 level was measured by an inverted fluorescence microscope system. Subsequently, the DCFH-DA was employed to detect the intracellular ROS. Briefly, 4T1 cells were incubated with a medium containing CAT@MnPFs (200 µg mL^{-1}) for 4 h, followed by washing with PBS and adding a fresh medium containing DCFH-DA. Then 4T1 cells were exposed to a 650 nm light (100 mW cm^{-2}) for 5 min. The 4T1 cells only treated with CAT@MnPFs were also conducted under the same conditions. Before imaging, the cells were stained with DAPI for 20 min.

2.7. PDT in vitro

4T1 cells were incubated with CAT@MnPFs (200 µg mL^{-1}) for 4 h. After removing the CAT@MnPFs solution, the treated cells were washed by PBS and exposed to a 650 nm light (100 mW cm^{-2}) for 10 min. Thereafter, the 4T1 cells were co-stained with Calcein AM and propidium iodide (PI) to visualize the phototoxicity of CAT@MnPFs. To study the effect of H_2O_2 on phototoxicity, 4T1 cells were co-incubated with CAT@MnPFs (200 µg mL^{-1}) and H_2O_2 (100 µM) for 4 h, followed by the irradiation of light for 5 min and the addition of Calcein AM/PI dye. Meanwhile, the 4T1 cells were only treated with CAT@MnPFs (200 µg mL^{-1}) in the absence of H_2O_2 and exposed to light. In addition, the cell viabilities were determined by CCK-8 assay.

2.8. Hemolysis

To obtain a fresh blood sample, the tails of mice were fixed on the operating table, disinfected, immersed in 45 °C water for 3 min, and cut off by 3 cm. The collected fresh blood was centrifugated at 2000 rpm for 20 min and washed with PBS three times, obtaining red blood cells (RBCs). Then the RBCs were diluted with PBS to a 2 % RBCs suspension. Samples (1 mL) in PBS at different concentrations (50, 100, 200, 300 µg mL^{-1}) were incubated with 2 % dilute RBCs at 37 °C for 30 min. For comparisons, 1 mL of water containing 2 % RBCs was a positive control, and 1 mL of PBS containing 2 % RBCs was a negative control. The positive and negative control groups were incubated at the same conditions for 30 min. Then all the groups were centrifuged at 10000 rpm for 20 min and their photoabsorptance of supernatants at 540 nm was measured by a microplate reader. The hemolysis rate was calculated according to the following formula: $(A_{sample}-A_{negative})/(A_{postive}-A_{negative}) \times 100$ %. To observe the morphology of RBCs, different samples after the incubation were dropped onto the slide and observed under an optical microscope.

2.9. Statistical analysis

In order to ensure the accuracy and reliability of the experiment, the experiments were repeated three times for statistical analysis to verify the results, and at least three replicates were performed for each test. Data were presented as the mean ± standard deviation. Multiple comparison tests were performed using one-way analysis of variance (ANOVA) and Tukey's post hoc test; comparisons between two groups were performed using two-tailed unpaired t-tests.

3. Results and discussion

3.1. Synthesis and characterizations of MnPFs

The MnPFs were synthesized through the assembly of organic linker PpIX and metal node Mn^{2+} ions through covalent interaction. In the structure of MnPFs, the carboxyl groups of PpIX are coordinated with Mn^{2+} ions, similar to traditional MOFs [26]. The transmission electron microscopy (TEM) images reveal that MnPFs have no regular size with an average size of ~114 nm (Fig. 1a and S1a in the supporting information). In the high solution TEM image, MnPFs have an amorphous structure on account of asymmetric carboxyl groups in PpIX (Fig. 1b), which is different from the typical crystalline MOFs [27]. After storage in PBS for 5 days, there is an unobvious change in size for the MnPFs sample, indicating good stability (Fig. S1b). According to elemental mapping, Mn and N elements were homogeneously distributed in the MnPFs, indicating that MnPFs are composed of Mn ions and PpIX linkers. To characterize the MnPFs, we further performed X-ray photoelectron spectroscopy (XPS), UV–vis spectra, and fluorescence spectra. The survey XPS spectrum shows the signal of C, N, O, and Mn elements, indicating the purity of MnPFs (Fig. S2 in supporting information). As shown in the high resolution of Mn 2p XPS spectrum, the Mn ions of MnPFs exhibit 641.8 eV and 653.7 eV peaks (Fig. 1d), which are ascribed to Mn $2p_{3/2}$ and Mn $2p_{1/2}$, respectively [28]. Additionally, the Mn $2p_{3/2}$ signal was deconvoluted into three peaks at 640.8, 641.8, and 643.5 eV, which were fitted to Mn(II) and satellite peaks. The aqueous solution containing MnPFs is dark red (Fig. S3). UV–vis spectra demonstrate that PpIX molecules have a strong characteristic absorption peak at 375 nm and four specific Q-bands from 522 to 662 nm (Fig. 1e). And MnPFs exhibit one redshift and widened strong peak at 380 nm and four characteristic absorption peaks at 522–662 nm, which have no essential difference from that of PpIX molecules. It should be noted that the specific absorption is ascribed to the π electrons on the ring [29]. The four Q-bands peaks indicate that Mn ions coordinate with the carboxyl of PpIX, rather than chelating into the porphyrin rings to form metalloporphyrin [30]. Under the excitation of the 400 nm light, the fluorescence
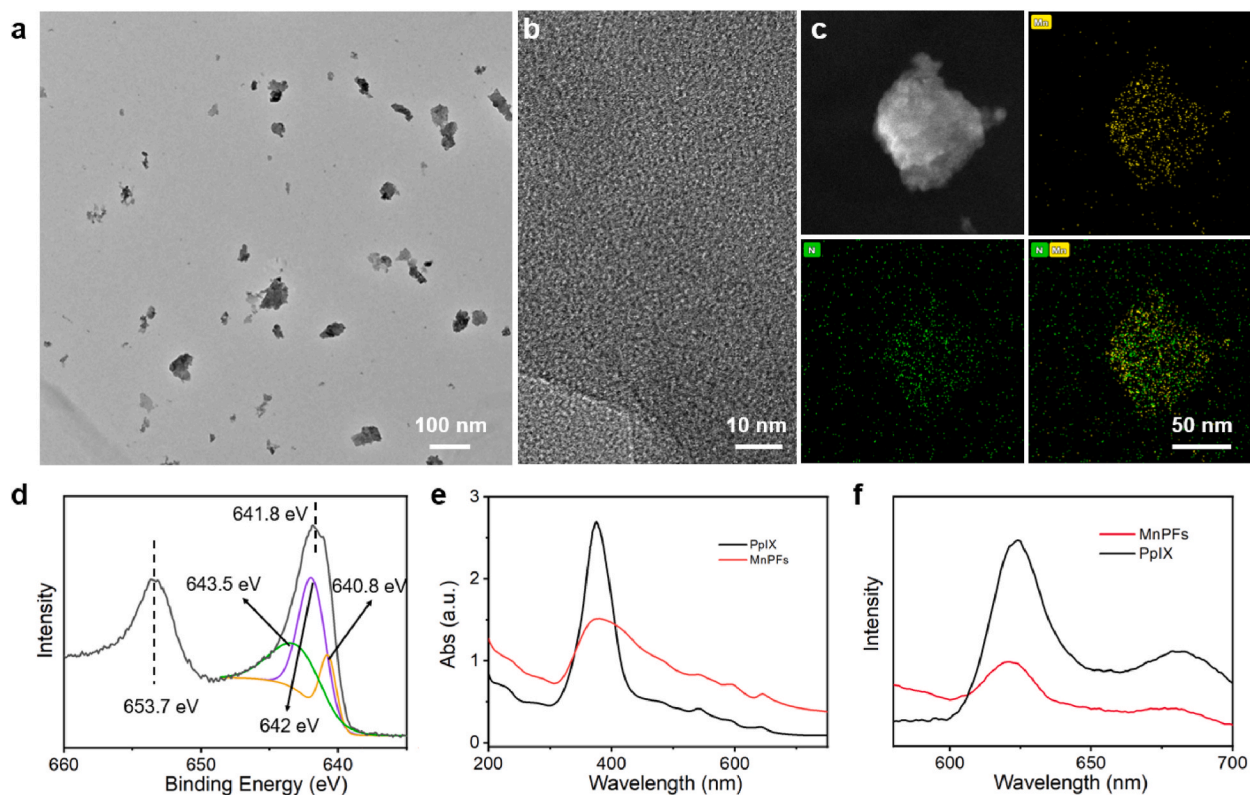

Fig. 1. TEM image (a), high-resolution TEM image (b), elemental mapping (c), and Mn 2p XPS spectrum (d) of MnPFs. UV–vis absorption spectra (e) and fluorescence spectra (f) of MnPFs and PpIX.

spectrum of MnPFs shows two emission peaks at 621 and 681 nm (Fig. 1f), which is similar to that of PpIX. These results proved that MnPFs were assembled through the coronation between Mn ions and PpIX.

3.2. Catalase loading and $^1O_2$ production

Then the obtained MnPFs were used to load the catalase, forming catalase-loaded MnPFs (CAT@MnPFs). To confirm the successful loading of catalase, we tested the changes in zeta potential before and after catalase loading. The zeta-potential of MnPFs is measured to −10.9 mV, while that of CAT@MnPFs decreases to −16.0 mV (Fig. 2a), which is attributed to negative charges of catalase, confirming the success of catalase loading. The catalytic activity of catalase was verified by the change of dissolved oxygen content, which was detected by a portable dissolved oxygen meter. H_2O_2 solution (1 mM) was introduced into the MnPFs (10 mL, 50 µg mL^{-1}) and CAT@MnPFs (10 mL, 50 µg mL^{-1}) solutions, respectively. After a reaction for 600s, MnPFs could not induce an obvious elevation in oxygen content in the presence of H_2O_2, while the O_2 concentration goes up rapidly in the CAT@MnPFs + H_2O_2 solution with a huge elevation (13.2 mg L^{-1}, Fig. 2b), indicating the good catalytic activity of catalase. It has been reported that Mn^{2+} ions can consume H_2O_2 to produce hydroxyl radicals through Fenton-like reactions, and this point is not emphasized due to the high catalytic efficacy of CAT and ROS production by light irradiation [31]. Thus, catalase was successfully loaded onto CAT@MnPFs and catalyzed H_2O_2 to generate O_2.

It has been reported that PpIX can cause serious cellular toxicity by producing $^1O_2$ under light irradiation, initiating necrosis and apoptosis [32]. It can be deduced that the PpIX in CAT@MnPFs can serve as photosensitizers to generate $^1O_2$ for PDT. To explore the PDT function of CAT@MnPFs, the $^1O_2$ production by CAT@MnPFs was measured with a 2,2,6,6-tetramethylpiperidine (TEMP) indicator. In the electron spin resonance (ESR) test, TEMP can capture $^1O_2$ and generate nitroxide radical 2,2,6,6-tetramethyl-1-piperidinyloxyl (TEMPOL) that is a paramagnetic product with unpaired electrons on the NO groups and has a characteristic 1:1:1 triple signal [33]. When the solution containing TEMP and CAT@MnPFs is excited by a 650 nm light, a characteristic $^1O_2$-induced strong 1:1:1 triple signal can be observed (Fig. 3a), verifying the $^1O_2$ production by CAT@MnPFs upon light irradiation.

To shed light on the ability of $^1O_2$ generation, DPBF, which could be degraded by $^1O_2$, was selected as a probe and mixed with CAT@MnPFs solution to measure the production of $^1O_2$ under 650 light stimulations. Under light irradiation, CAT@MnPFs trigger the decrease in the characteristic absorption peaks of DPBF at 410 nm with the increase of time in the range of 0–30 s (Fig. 3b), indicating the generation of $^1O_2$. At 30 s, the degradation rate of DPBF is determined to be 19.1 %. Moreover, compared to the CAT@MnPFs + light group, the degradation rate can be accelerated in the presence of H_2O_2 (1 mM), and the degradation efficiency is 55.0 % at 30 s (Fig. 3c and d). As shown in Fig. 3d, the degradation efficiency of CAT@MnPFs + light in the presence of H_2O_2 is nearly three times that (19.1 %) of CAT@MnPFs + light group. The faster degradation should be ascribed to catalase catalyzing the production of oxygen. Thus, these results proved that CAT@MnPFs could serve as catalase-assisted photosensitizers to achieve PDT functions.

Biocompatibility of CAT@MnPFs is a prerequisite for further applications of photosensitizers. The cytotoxicity of CAT@MnP in darkness was studied by a standard CCK-8 assay. In the dark, 4T1 cells were incubated with CAT@MnP at a series of concentrations (0–300 µg mL^{-1}). After 24 h of incubation, the cell viability remains ~90 % even at a high concentration of up to 300 µg mL^{-1} (Fig. 4a), showing low cytotoxicity. The low cytotoxicity indicates that CAT@MnPFs with good biocompatibility are the potential photosensitizers. Subsequently, the endocytosis was confirmed after incubating CAT@MnPFs (200 µg mL^{-1}) for various durations (0.5, 1, 3, 4 h). As shown in Figs. 4b and 3, a red fluorescence signal occupied cells when CAT@MnPFs are incubated for 0.5 h. With time prolonging, the signal disperses within the cytoplasm and enhances in intensity (Fig. 4c), demonstrating that CAT@MnPFs are able to efficiently enter the cancer cells in a time-dependent manner.

Hypoxia is a high characteristic of TME, which would hinder the process of oxygen-dependent PDT. The loaded catalase can trigger the decomposition of endogenous H_2O_2 into O_2 for hypoxic alleviation. [Ru(dpp)$_3$]Cl$_2$ is an oxygen indicator whose red fluorescence
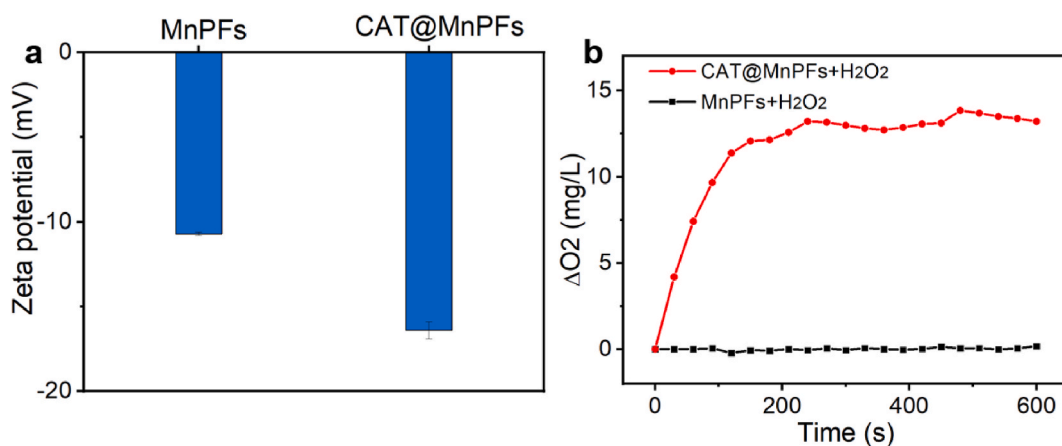

Fig. 2. (a) zeta potential of MnPFs and CAT@MnPFs. (b) Dissolved O_2 concentration changes for MnPFs and CAT@MnPFs samples in the presence of H_2O_2.
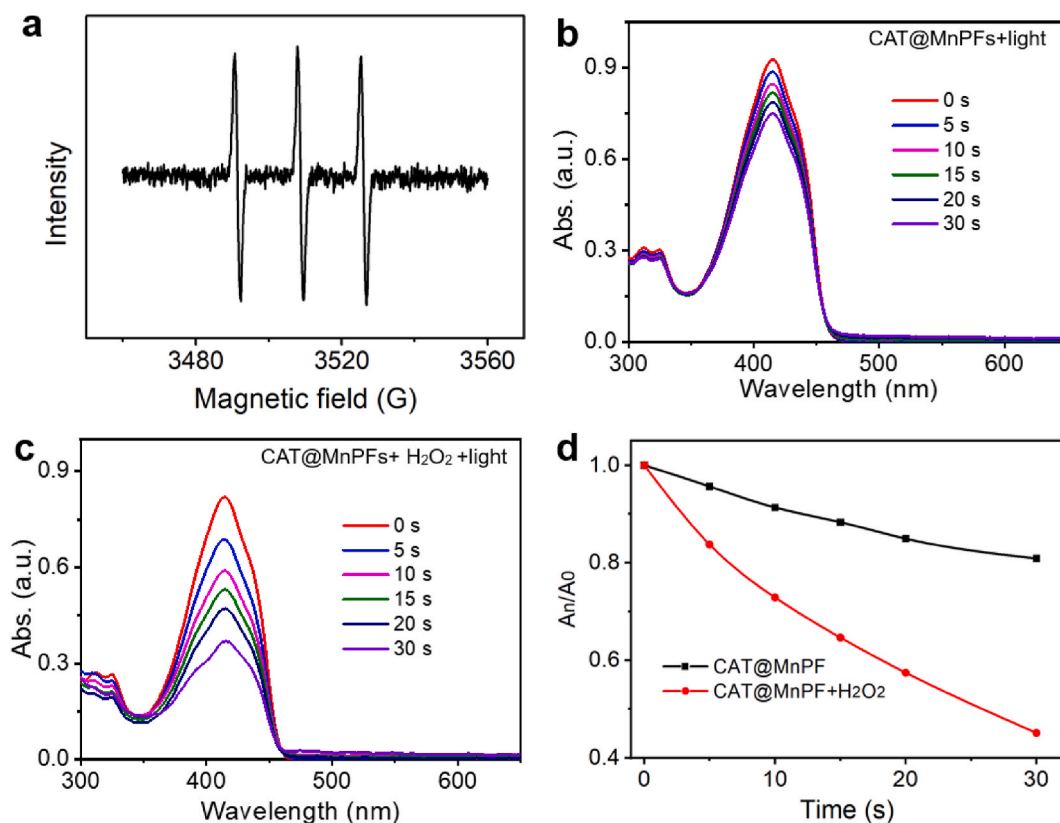
Fig. 3. (a) ESR signal of $^1O_2$ for light-induced CAT@MnPFs. The oxidation spectra of DPBF solution containg CAT@MnPFs (b) and CAT@MnPFs + H_2O_2 (c) under light irradiation. (d) The oxidation rate after different treatments.

can be quenched by O_2 [34]. To evaluate the catalytic performance, the $[Ru(dpp)_3]_3Cl_2$ was employed to incubate with 4T1 cells to test the intracellular hypoxia level. As expected, 4T1 cells without any treatment exhibit bright red fluorescence in the hypoxia condition, while the cells treated with CAT@MnPFs (200 μg mL^{-1}) show no obvious fluorescent signal (Fig. 4d), proving that CAT@MnPFs improve the intracellular oxygen level because of the catalase activity.

The high degradation rate to DPBF and effective O_2 production prompt us to further evaluate the phototoxicity of CAT@MnPFs. To elucidate the intracellular mechanism of CAT@MnPFs as photosensitizers in phototoxicity, DCFH-DA was employed to detect the intracellular ROS levels. The newly generated reactive oxygen (ROS) can convert non-fluorescent DAFH-DA to 2′,7′-dichlorofluorescein (DCF) which emits strong green fluorescence. The 4T1 cells were co-treated with CAT@MnPFs (200 μg mL^{-1}) and DCFH-DA, then exposed to a 650 nm light for 10 min. As clearly shown in Fig. 5, the cells in the CAT@MnPFs group exhibit an inconspicuous green fluorescence signal, similar to the control group (only treated with light irradiation), indicating the absence of ROS. This similarity may be due to the low ROS generation by intracellular CAT@MnPFs and the redox balance capacity of cells. Interestingly, some strong fluorescence signals can be found after simultaneously treating with CAT@MnPFs and light irradiation, proving that the ROS is triggered by CAT@MnPFs under light exposure. To further confirm the phototoxicity, the cell-killing effect of CAT@MnPFs under the light was visualized by co-staining with calcein AM/PI which can stain the live cells with green fluorescence and dead cells with red fluorescence. The region without light irradiation manifests strong green fluorescence and neglectable red fluorescence (Fig. 6a). On the contrary, after exposure to 650 nm light for 10 min, the cells show a red fluorescence signal in the light irradiation region. Cell death derives from the $^1O_2$ oxidation produced by CAT@MnPFs upon light exposure, namely the phototoxicity of CAT@MnPFs.

To study the effect of catalase activity on therapeutical effect, 4T1 were incubated with CAT@MnPFs (200 μg mL^{-1}) for 4 h, followed by light irradiation for 5 min. Considering the high endogenous H_2O_2 in tumors, additional H_2O_2 (100 μM) was added to the culture medium to simulate the tumor microenvironment [35]. The image of the CAT@MnPFs + light group shows not only red fluorescence but also green fluorescence (Fig. 6b), indicating the destroy of part of the cells. Moreover, in the presence of H_2O_2, the cells almost emit red fluorescence due to cell proliferation suppression and massive cell death. The high therapeutic efficiency means that the loaded catalase facilitates the killing cells process through hypoxic alleviation of TME. CCK-8 assay results demonstrate a similar therapeutic tendency with cell viability of 49.6 % in the CAT@MnPFs + light group and 19.9 % in the CAT@MnPFs + light + H_2O_2 group (Fig. 6c), suggesting that CAT@MnPFs feature catalytically-assisted PDT functions.

Hemocompatibility is a critical parameter to assess the most of biomaterials for further biomedical applications [36]. For the compatibility of the CAT@MnPFs assay, the hemolysis rate was studied in a 2 % red blood cells (RBCs) suspension [37]. A series of
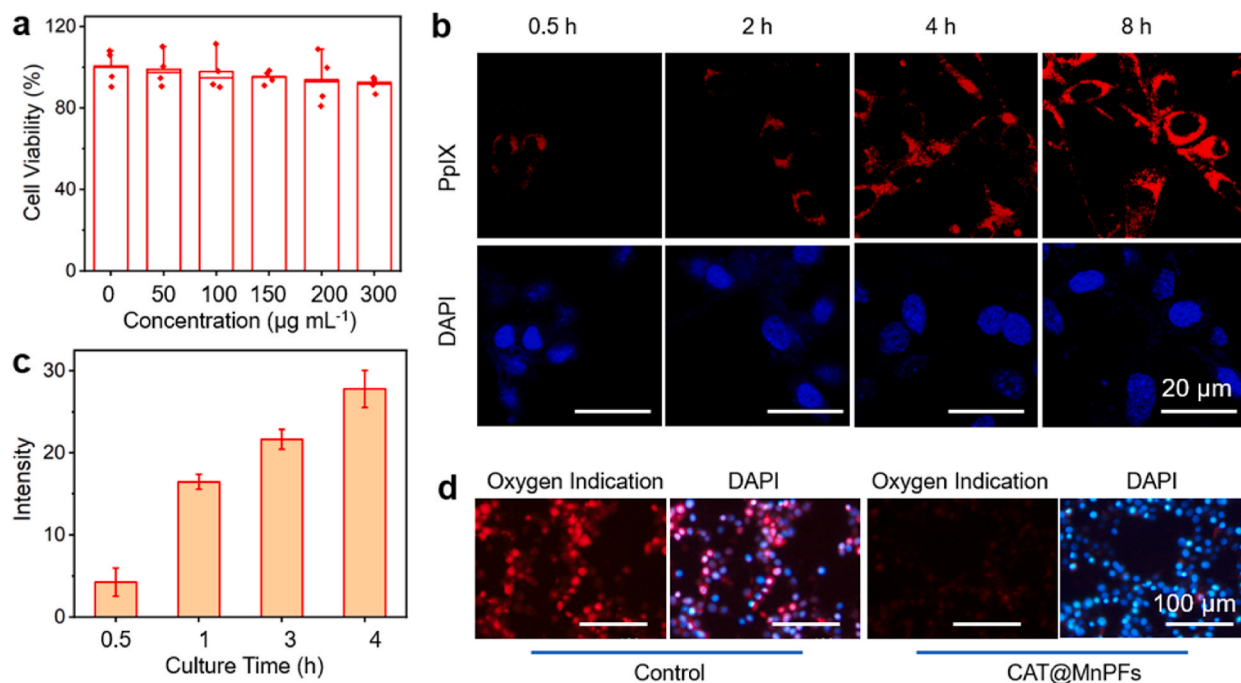
Fig. 4. (a) Viability of 4T1 cells with CAT@MnPFs at 0–300 μg mL^{-1} for 24 h. (b) Confocal images of cells incubated with CAT@MnPFs for different time. (c) Semi-quantitative analysis of PpIX fluorescence signals. (d) Fluorescence images of 4T1 cells stained with oxygen indicator [Ru(dpp)$_3$]Cl$_2$ and DAPI.
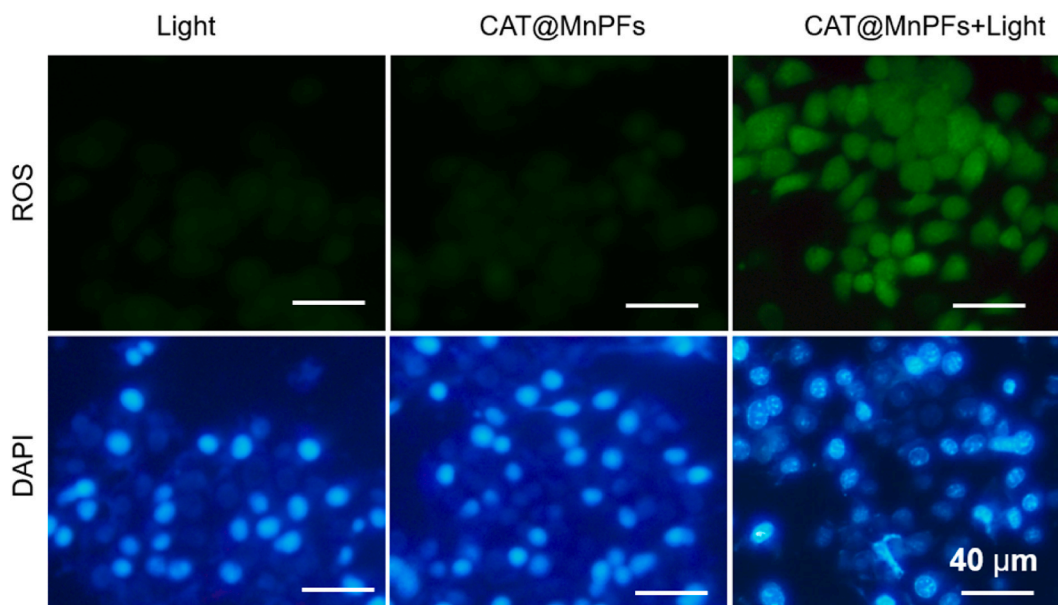

Fig. 5. Fluorescence images of 4T1 cells stained with DCFH-DA assay for intracellular ROS detection.

CAT@MnPFs concentrations were incubated with 2 % RBCs at 37 °C for 30 min. Indistinct hemolysis could not be found in the negative control, whereas water (positive control) induced obvious hemolysis (Fig. 7a). The hemolysis percentage of CAT@MnPFs was determined to be less than 6 % at concentrations ≤300 μg mL^{-1}. Meanwhile, the morphologies of RBCs were normal in the CAT@MnPFs groups (Fig. 7b), which is similar to the negative control group, suggesting that CAT@MnPFs could not induce little damage to RBCs. Taken together, it can be concluded that CAT@MnPFs features favorable biocompatibility and biosafety.
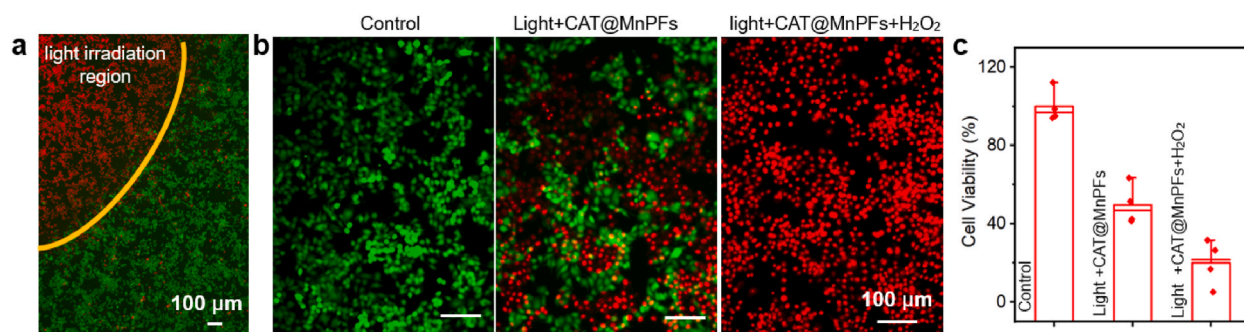
Fig. 6. (a) 4T1 cells stained with calcein AM/PI after the incubation with CAT@MnPFs and irradiation by light for 10 min. Fluorescence images (b) and cell viability (c) of 4T1 cells after different treatments.
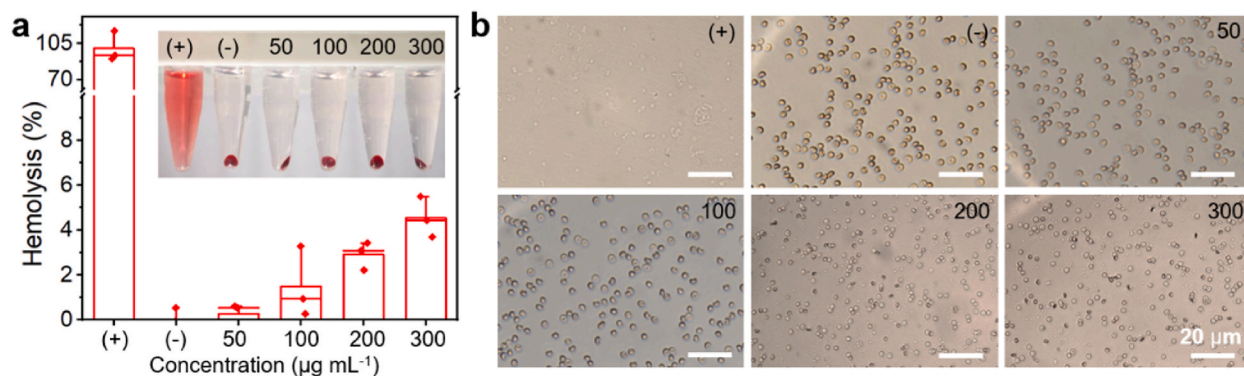

Fig. 7. (a) Hemolysis ratio of RBCs after incubation with CAT@MnPFs at different concentrations (50–300 μg mL^{-1}). Water is a positive control group and PBS is the negative control group. Inset: Photographs of hemolysis assay. (b) Optical microscopic images of RBCs after incubation with different samples.

4. Conclusions

In summary, the multifunctional CAT@MnPFs were developed to generate O_2 for boosting PDT. The CAT@MnPFs were obtained by the assembly of Mn^{2+} and PpIX via covalent coordination, and then the loading with catalase. The CAT@MnPFs with an amorphous structure have an average size of ~114 nm and exhibit a high $^1O_2$ generation rate. In addition, the loaded CAT is able to catalyze the decomposition of H_2O_2 to induce a huge O_2 elevation (13.22 mg L^{-1}) in 600 s, leading to enhanced generation of $^1O_2$. When CAT@MnPFs were incubated with 4T1 cells, cells could be killed by CAT@MnPFs under the 650 nm light exposure due to $^1O_2$ oxidation. Meanwhile, CAT@MnPFs only induce negligible hemolysis even at 300 μg mL^{-1}, showing their high biosafety. Therefore, this work could provide insights into the design of photosensitizers to address the hypoxia in tumors. In our future work, we will optimize CAT@MnPFs by conjugating tumor-targeting molecules, studying the therapeutic effects and antitumor mechnism on a metastatic tumor model.

CRediT authorship contribution statement

Yang Qiao: Writing – original draft. **Xiaowan Tang:** Validation, Software, Investigation. **Xu Qiuju:** Writing – review & editing. **Guangwen Zhang:** Project administration, Funding acquisition.

Declaration of competing interest

The authors declare the following financial interests/personal relationships which may be considered as potential competing interests: Qiao Yang reports financial support was provided by Taizhou Science and Technology Bureau project 23ywa29. Guangwen Zhang reports financial support was provided by Taizhou Science and Technology Bureau project 1901ky56. If there are other authors, they declare that they have no known competing financial interests or personal relationships that could have appeared to influence the work reported in this paper.

Acknowledgments

Appendix A. Supplementary data

Supplementary data to this article can be found online at https://doi.org/10.1016/j.heliyon.2024.e33902.

References

[1] Y.Y. Li, X.B. Zhang, Y. Zhang, Y.L. He, Y. Liu, H.X. Ju, Activatable photodynamic therapy with therapeutic effect prediction based on a self-correction upconversion nanoprobe, ACS Appl. Mater. Interfaces 12 (17) (2020) 19313–19323, https://doi.org/10.1021/acsami.0c03432.
[2] V.G. Deepagan, D.G. You, W. Um, H. Ko, S. Kwon, K.Y. Choi, G.R. Yi, J.Y. Lee, D.S. Lee, K. Kim, I.C. Kwon, J.H. Park, Long-circulating Au-TiO₂ nanocomposite as a sonosensitizer for ROS-mediated eradication of cancer, Nano Lett. 16 (10) (2016) 6257–6264, https://doi.org/10.1021/acs.nanolett.6b02547.
[3] F. Gong, L. Cheng, N. Yang, O. Betzer, L. Feng, Q. Zhou, Y. Li, R. Chen, R. Popovtzer, Z. Liu, Ultrasmall oxygen-deficient bimetallic oxide MnWOₓ nanoparticles for depletion of endogenous GSH and enhanced sonodynamic cancer therapy, Adv. Mater. 31 (23) (2019) 1900730, https://doi.org/10.1002/adma.201900730, 1900730.
[4] P. Huang, X. Qian, Y. Chen, L. Yu, H. Lin, L. Wang, Y. Zhu, J. Shi, Metalloporphyrin-encapsulated biodegradable nanosystems for highly efficient magnetic resonance imaging-guided sonodynamic cancer therapy, J. Am. Chem. Soc. 139 (3) (2017) 1275–1284, https://doi.org/10.1021/jacs.6b11846.
[5] H.J. Chen, X.R. Huang, X.B. Zhou, B.Y. Zheng, J.D. Huang, Potential sonodynamic anticancer activities of artemether and liposome-encapsulated artemether, Chem. Commun. 51 (22) (2015) 4681–4684, https://doi.org/10.1039/c5cc00927h.
[6] Y. Wang, L. Shi, D. Ma, S. Xu, W. Wu, L. Xu, M. Panahandeh-Fard, X. Zhu, B. Wang, B. Liu, Tumor-activated and metal–organic framework assisted self-assembly of organic photosensitizers, ACS Nano (2020), https://doi.org/10.1021/acsnano.0c04518.
[7] Y. Yang, J.X. Liang, L. Feng, F. Fu, Z. Dong, Y. Chao, Y. Li, G. Lu, M. Chen, Z. Liu, Nanoscale metal-organic particles with rapid clearance for magnetic resonance imaging-guided photothermal therapy, ACS Nano 10 (2) (2016) 2774–2781, https://doi.org/10.1021/acsnano.5b07882.
[8] Z. Jiang, X. Han, Y. Du, Y. Li, Y. Li, J. Li, J. Tian, A. Wu, Mixed metal metal–organic frameworks derived carbon supporting ZnFe₂O₄/C for high-performance magnetic particle imaging, Nano Lett. 21 (7) (2021) 2730–2737, https://doi.org/10.1021/acs.nanolett.0c04455.
[9] X. Han, Y. Li, Y. Zhou, Z. Song, Y. Deng, J. Qin, Z. Jiang, Metal-organic frameworks-derived bimetallic nanozyme platform enhances cytotoxic effect of photodynamic therapy in hypoxic cancer cells, Mater. Des. 204 (2021) 109646, https://doi.org/10.1016/j.matdes.2021.109646.
[10] T. Zhang, Y. Sun, J. Cao, J. Luo, J. Wang, Z. Jiang, P. Huang, Intrinsic nucleus-targeted ultra-small metal–organic framework for the type I sonodynamic treatment of orthotopic pancreatic carcinoma, J. Nanobiotechnol. 19 (1) (2021), https://doi.org/10.1186/s12951-021-01060-7.
[11] M. Wen, N. Yu, Z. Yi, P. Qiu, C. Tao, D.K. Macharia, M. Zhu, Z. Chen, X. Liu, On-demand phototoxicity inhibition of sensitizers and H₂S-triggered in-situ activation for precise therapy of colon cancer, Nano Today 50 (2023) 101863, https://doi.org/10.1016/j.nantod.2023.101863.
[12] B. Li, X. Lu, Y. Tian, D. Li, Embedding multiphoton active units within metal–organic frameworks for turning on high-order multiphoton excited fluorescence for bioimaging, Angew. Chem. Int. Ed. 61 (31) (2022) e202206755, https://doi.org/10.1002/anie.202206755.
[13] D. Zhang, Z. Ye, L. Wei, H. Luo, L. Xiao, Cell membrane-coated porphyrin metal–organic frameworks for cancer cell targeting and O₂-evolving photodynamic therapy, ACS Appl. Mater. Interfaces 11 (43) (2019) 39594–39602, https://doi.org/10.1021/acsami.9b14084.
[14] M. He, Y. Chen, C. Tao, Q. Tian, L. An, J. Lin, Q. Tian, H. Yang, S. Yang, Mn–porphyrin-based metal–organic framework with high longitudinal relaxivity for magnetic resonance imaging guidance and oxygen self-supplementing photodynamic therapy, ACS Appl. Mater. Interfaces 11 (45) (2019) 41946–41956, https://doi.org/10.1021/acsami.9b15083.
[15] D. Hu, L. Zhong, M. Wang, H. Li, Y. Qu, Q. Liu, R. Han, L. Yuan, K. Shi, J. Peng, Z. Qian, Perfluorocarbon-loaded and redox-activatable photosensitizing agent with oxygen supply for enhancement of fluorescence/photoacoustic imaging guided tumor photodynamic therapy, Adv. Funct. Mater. 29 (9) (2019) 1806199, https://doi.org/10.1002/adfm.201806199.
[16] J. Xiang, X. Yang, M. Tan, J. Guo, Y. Ye, J. Deng, Z. Huang, H. Wang, W. Su, J. Cheng, L. Zheng, S. Liu, J. Zhong, J. Zhao, NIR-enhanced Pt single atom/g-C₃N₄ nanozymes as SOD/CAT mimics to rescue ATP energy crisis by regulating oxidative phosphorylation pathway for delaying osteoarthritis progression, Bioact. Mater. 36 (2024) 1–13, https://doi.org/10.1016/j.bioactmat.2024.02.018.
[17] G. Xu, K. Liu, B. Jia, Z. Dong, C. Zhang, X. Liu, Y. Qu, W. Li, M. Zhao, H. Zhou, Y. Li, Electron lock manipulates the catalytic selectivity of nanozyme, ACS Nano 18 (4) (2024) 3814–3825, https://doi.org/10.1021/acsnano.3c12201.
[18] J. Huang, X. Jia, Y. Wang, Y. Qiao, X. Jiang, Heterojunction-mediated co-adjustment of band structure and valence state for achieving selective regulation of semiconductor nanozymes, Adv. Healthcare Mater. (2024) 2400401, https://doi.org/10.1002/adhm.202400401.
[19] X. Li, Y. Pan, J. Zhou, G. Yi, C. He, Z. Zhao, Y. Zhang, Hyaluronic acid-modified manganese dioxide-enveloped hollow copper sulfide nanoparticles as a multifunctional system for the co-delivery of chemotherapeutic drugs and photosensitizers for efficient synergistic antitumor treatments, J. Colloid Interface Sci. 605 (2022) 296–310, https://doi.org/10.1016/j.jcis.2021.07.092.
[20] M. Wang, M.Y. Chang, Q. Chen, D.M. Wang, C.X. Li, Z.Y. Hou, J. Lin, D.Y. Jin, B.G. Xing, Au₂Pt-PEG-Ce6 nanoformulation with dual nanozyme activities for synergistic chemodynamic therapy/phototherapy, Biomaterials 252 (2020) 12, https://doi.org/10.1016/j.biomaterials.2020.120093.
[21] T. Zhu, L. Shi, C. Ma, L. Xu, J. Yang, G. Zhou, X. Zhu, L. Shen, Fluorinated chitosan-mediated intracellular catalase delivery for enhanced photodynamic therapy of oral cancer, Biomater. Sci. 9 (3) (2021) 658–662, https://doi.org/10.1039/D0BM01898H.
[22] H. Wang, Y. Chao, J. Liu, W. Zhu, G. Wang, L. Xu, Z. Liu, Photosensitizer-crosslinked in-situ polymerization on catalase for tumor hypoxia modulation & enhanced photodynamic therapy, Biomaterials 181 (2018) 310–317, https://doi.org/10.1016/j.biomaterials.2018.08.011.
[23] S.Z.F. Phua, G. Yang, W.Q. Lim, A. Verma, H. Chen, T. Thanabalu, Y. Zhao, Catalase-integrated hyaluronic acid as nanocarriers for enhanced photodynamic therapy in solid tumor, ACS Nano 13 (4) (2019) 4742–4751, https://doi.org/10.1021/acsnano.9b01087.
[24] L. Cheng, D. Jiang, A. Kamkaew, H.F. Valdovinos, H.-J. Im, L. Feng, C.G. England, S. Goel, T.E. Barnhart, Z. Liu, W. Cai, Renal-clearable PEGylated porphyrin nanoparticles for image-guided photodynamic cancer therapy, Adv. Funct. Mater. 27 (34) (2017), https://doi.org/10.1002/adfm.201702928.
[25] H. Xu, N. Yu, J. Zhang, Z. Wang, P. Geng, M. Wen, M. Li, H. Zhang, Z. Chen, Biocompatible Fe-Hematoporphyrin coordination nanoplatforms with efficient sonodynamic-chemo effects on deep-seated tumors, Biomaterials 257 (2020) 120239, https://doi.org/10.1016/j.biomaterials.2020.120239.
[26] M. Wen, J. Shen, Z. Wang, H. Guo, P. Geng, N. Yu, M. Li, H. Zhang, M. Zhu, Z. Chen, A cascaded enzyme-loaded Fe–hemoporfin framework for synergistic sonodynamic-starvation therapy of tumors, Nanoscale 13 (11) (2021) 5910–5920, https://doi.org/10.1039/D0NR08508A.
[27] J.-H. Dou, M.Q. Arguilla, Y. Luo, J. Li, W. Zhang, L. Sun, J.L. Mancuso, L. Yang, T. Chen, L.R. Parent, G. Skorupskii, N.J. Libretto, C. Sun, M.C. Yang, P.V. Dip, E. J. Brignole, J.T. Miller, J. Kong, C.H. Hendon, J. Sun, M. Dincă, Atomically precise single-crystal structures of electrically conducting 2D metal–organic frameworks, Nat. Mater. 20 (2) (2021) 222–228, https://doi.org/10.1038/s41563-020-00847-7.
[28] X. Zhong, Z. Lu, W. Liang, B. Hu, Incorporating bimetal oxide MnFe₂O₄ onto covalent organic frameworks for the removal of UO2²⁺ ion from aqueous solution, Appl. Surf. Sci. 556 (2021) 149581, https://doi.org/10.1016/j.apsusc.2021.149581.

[29] P. Huang, X. Qian, Y. Chen, L. Yu, H. Lin, L. Wang, Y. Zhu, J. Shi, Metalloporphyrin-encapsulated biodegradable nanosystems for highly efficient magnetic resonance imaging-guided sonodynamic cancer therapy, J. Am. Chem. Soc. 139 (3) (2017) 1275–1284, https://doi.org/10.1021/jacs.6b11846.

[30] S.A. Younis, D.-K. Lim, K.-H. Kim, A. Deep, Metalloporphyrinic metal-organic frameworks: Controlled synthesis for catalytic applications in environmental and biological media, Adv Colloid Interfac 277 (2020) 102108, https://doi.org/10.1016/j.cis.2020.102108.

[31] Q. Chen, Y. Ma, P. Bai, Q. Li, B.S.B. Canup, D. Long, B. Ke, F. Dai, B. Xiao, C. Li, Tumor microenvironment-responsive nanococktails for synergistic enhancement of cancer treatment via cascade reactions, ACS Appl. Mater. Interfaces 13 (4) (2021) 4861–4873, https://doi.org/10.1021/acsami.0c20268.

[32] B. Qiao, Y. Luo, H.-B. Cheng, J. Ren, J. Cao, C. Yang, B. Liang, A. Yang, X. Yuan, J. Li, L. Deng, P. Li, H.-T. Ran, L. Hao, Z. Zhou, M. Li, Y. Zhang, P.S. Timashev, X.-J. Liang, Z. Wang, Artificial nano-targeted cells (ANTC) with stable photothermal performance for multimodal imaging-guided tumor-specific therapy, ACS Nano (2020), https://doi.org/10.1021/acsnano.0c00771.

[33] A. Ma, H. Chen, Y. Cui, Z. Luo, R. Liang, Z. Wu, Z. Chen, T. Yin, J. Ni, M. Zheng, L. Cai, Metalloporphyrin complex-based nanosonosensitizers for deep-tissue tumor theranostics by noninvasive sonodynamic therapy, Small 15 (5) (2019) 1804028, https://doi.org/10.1002/smll.201804028.

[34] M. Wen, N. Yu, S. Wu, M. Huang, P. Qiu, Q. Ren, M. Zhu, Z. Chen, On-demand assembly of polymeric nanoparticles for longer-blood-circulation and disassembly in tumor for boosting sonodynamic therapy, Bioact. Mater. 18 (2022) 242–253, https://doi.org/10.1016/j.bioactmat.2022.03.009.

[35] Z. Chu, J. Yang, W. Zheng, J. Sun, W. Wang, H. Qian, Recent advances on modulation of H_2O_2 in tumor microenvironment for enhanced cancer therapeutic efficacy, Coord. Chem. Rev. 481 (2023) 215049, https://doi.org/10.1016/j.ccr.2023.215049.

[36] M. Li, Y. Gao, Y. Yuan, Y. Wu, Z. Song, B.Z. Tang, B. Liu, Q.C. Zheng, One-step formulation of targeted aggregation-induced emission dots for image-guided photodynamic therapy of cholangiocarcinoma, ACS Nano 11 (4) (2017) 3922–3932, https://doi.org/10.1021/acsnano.7b00312.

[37] F. Zhang, Y. Liu, J. Lei, S. Wang, X. Ji, H. Liu, Q. Yang, Metal–organic-framework-derived carbon nanostructures for site-specific dual-modality photothermal/photodynamic thrombus therapy, Adv. Sci. 6 (17) (2019) 1901378, https://doi.org/10.1002/advs.201901378.